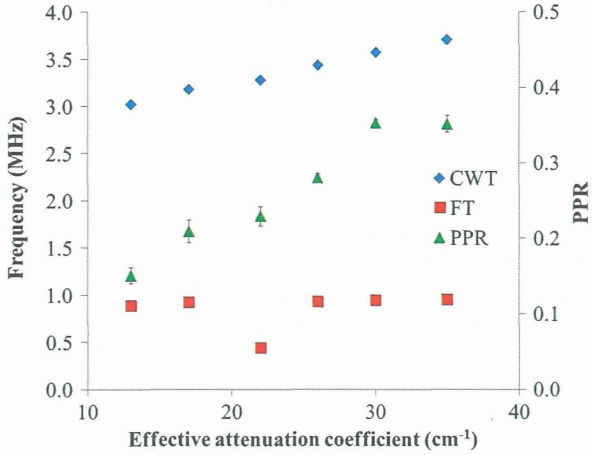

Fig. 8. Relationship between the maximum values of the dominant frequencies of the experimentally measured PA signals and the effective attenuation coefficients of optical absorbers (blue, triangle). The peak frequencies of power spectra calculated using FT (red, square) and PPR calculated from temporal waveform (green, triangle) are also plotted (error bar: standard deviation, $n = 4$).

The effective attenuation coefficients were determined using both the PPRs and the maximum value of the dominant frequencies. The relationship between both parameters and the effective attenuation coefficients obtained from the simulation was used to quantify the optical attenuation coefficient obtained experimentally from both parameters. Figure 9 compares the effective attenuation coefficients quantified using the CWT and spectrophotometer measurement. The linearity of the curve indicates agreement between two measurement methods. The mean square error of the spectrophotometer measurements was 2.0 cm^{-1}, whereas the uncertainties of the measurements calculated from the standard deviations of the maximum values of the dominant frequencies were less than 1.3 cm^{-1}. The effective attenuation

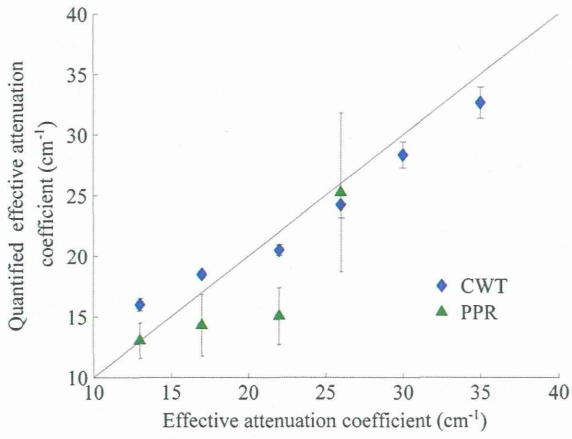

Fig. 9. Effective attenuation coefficients of the optical absorbers calculated from experimentally measured PA signals using CWT (blue, diamond) and temporal waveform (green, triangle) as a function of measured by spectrophotometer. The ideal fit line is also plotted (black, dotted) (error bar: standard deviation, $n = 4$).

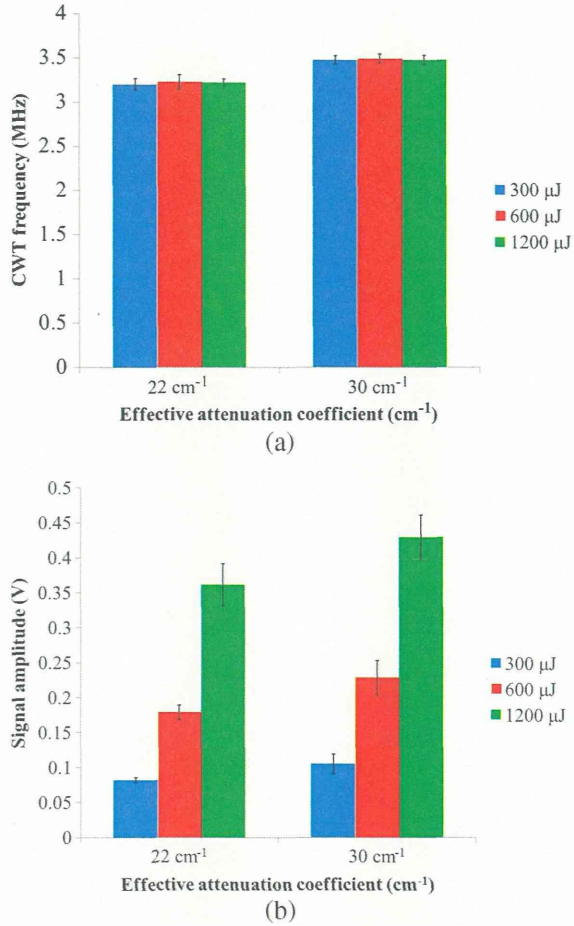

Fig. 10. (a) Maximum values of the dominant frequencies and (b) amplitude of PA signals produced from optical absorbers with effective attenuation coefficients of 22 and 30 cm^{-1}. The pulse energy of the excitation pulse was 300, 600, and 1200 μJ.

coefficients calculated from the PPRs are also shown in Fig. 9. Because the relationship between the PPR and the effective attenuation coefficient displayed in Fig. 5 was constant for coefficients larger than 30 cm^{-1}, we excluded these data points. The mean square error of the coefficients calculated from the PPRs was 3.7 cm^{-1}.

The maximum values of the dominant frequencies and the amplitudes of PA signals measured at various excitation pulse energies are shown in Figs. 10(a) and 10(b), respectively. Although the amplitude of the PA signal was proportional to the excitation pulse energy, the maximum value of the dominant frequency was constant for various excitation energies.

5. Discussion

This study shows that the maximum values of the dominant frequencies of PA signals obtained by CWT accurately represent the effective attenuation coefficients of optical absorbers.

The experimental and simulation results of this study suggest that the temporal resolution of the CWT makes the quantification method more robust

than that using the FT. The peak frequencies of the power spectra of the measured PA signals shown in Fig. 8 deviate from a linear relationship with the effective attenuation coefficients at the coefficients of 13 and 17 cm^{-1}. These deviations were caused by the variation in the acoustic sensor sensitivity at frequencies of less than 1 MHz. Since the FT calculates the frequency spectra without time resolution, the negative part of the PA signals that has long time duration dominates the frequency spectra. Since the negative part of PA signals consists of low frequency content, the peak frequency was strongly affected by the variation in the acoustic sensor sensitivity at frequencies of less than 1 MHz. In using CWT, the maximum values of the dominant frequencies will be less affected by the variation in the acoustic sensor sensitivity at frequencies of less than 1 MHz. This is because CWT divided the frequency contents of the positive and negative parts of the PA signals, and the frequency content of the positive part was selectively extracted.

The simulation and experimental results of this study also suggest that the CWT exhibits greater robustness than the PPR to distortions of the waveforms due to the detector impulse response functions. Another group proposed using the PPR calculated from the temporal waveform for quantification of the optical absorption coefficient using a forward-mode PA measurement system. In this study, we adopted this method for the reflection mode PA measurement system. In the reflection mode system, the negative peak of the PA signal was strongly affected by distortion due to the impulse response of the acoustic sensor, because it overlapped the residual oscillation of strong positive peak. Because the intensity of the negative peak was dominated by the residual oscillation of the positive peak, the PPR became constant for an effective attenuation coefficient larger than 30 cm^{-1} in the simulated result shown in Fig. 5.

We quantified the effective attenuation coefficient of a phantom made of diluted black ink by comparing the maximum values of the dominant frequencies calculated from the measured PA signal and from simulated PA signals. As shown in Fig. 9, we were able to calculate this value to within an error of 2.0 cm^{-1}. The calculated accuracy of the blood oxygen saturation depends on the difference in the effective attenuation coefficient between oxygenated and deoxygenated blood. This difference is known to be wavelength dependent, with a peak at 756 nm; by using excitation light at this wavelength, therefore, the blood oxygen saturation can be calculated accurately. At a wavelength of 756 nm, the effective attenuation coefficients of blood with oxygen saturation levels of 2.3% and 99.6% are 27.5 and 20.0 cm^{-1}, respectively, [3]. As the effective attenuation coefficient of the data set used to determine these values varies at a rate of -0.077 $cm^{-1}/\%$, a 2.0 cm^{-1} mean square error in the effective attenuation coefficient corresponds to a 24% error in the oxygen saturation. This error can be reduced by measuring the effective attenuation coefficient at multiple excitation wavelengths.

Because the CWT-based method uses frequency instead of amplitude to quantify the effective attenuation coefficient of an optical absorber, its results are expected to be independent of the optical fluence on the surface of the absorber. The results shown in Fig. 9 experimentally prove that the maximum value of the PA signal is independent of the excitation pulse energy; thus the parameter enables quantification of the effective attenuation coefficient without compensating for the optical fluence.

The challenges of the proposed method are the effects of the excitation beam profile and optical absorber shape on the dominant frequency of the PA signals. The dependence of the maximum value of the dominant frequency on the beam profile and the beam diameter on the optical absorber surface is shown in Fig. 11. The impulse response of the acoustic sensor was not incorporated into this simulation. The maximum values of the dominant frequency decrease as the beam diameter expands. The dominant frequency of the PA signals depends on both the leading and trailing edges of their temporal waveforms of PA signals. These waveforms of PA signals are determined by the spatial distribution of the optical energy absorption within the sensitive volume of an acoustic sensor. Because we used the unfocused acoustic sensor with a large sensitive volume, the spatial distribution of the optical energy determined by both the diameter and shape of the excitation beam directly affects the dominant frequency.

If the sensitive volume of the acoustic sensor is smaller than the spatial distribution of the optical absorption, the temporal waveforms of the PA signals are less sensitive to the beam diameter. Thus, focused acoustic sensors with a focused sensitive volume can be used to reduce the effects of both the profile and the diameter of the excitation beam.

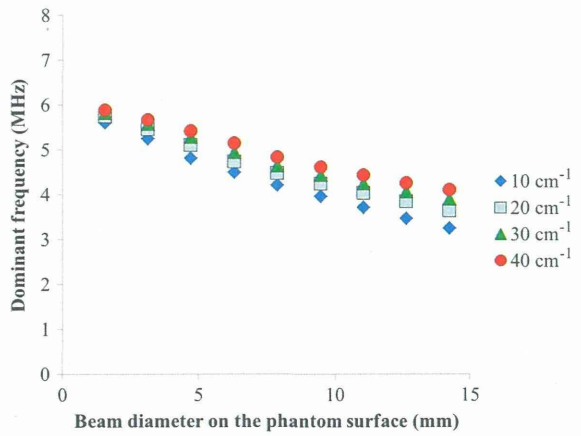

Fig. 11. Maximum value of the dominant frequency of simulated PA signals using ideal acoustic sensor as a function of the beam diameter on the surface of the optical absorber.

The use of focused acoustic sensors also reduces the effect of the optical absorber shape. If the optical absorber is sufficiently larger than the sensitive volume of the acoustic sensor, the surface of the optical absorber can be treated as a flat surface [9,13].

In this study, the proposed method was tested using the simplest model: a planar phantom placed in nonscattering media. If optical scattering is present, the proposed method suffers from two problems. One is the expansion of the spatial distribution of excitation light due to optical scattering. Because this problem is similar to the effect of the diameter and profile of the excitation beam, it is possible to reduce it by using a focused acoustic sensor. We are currently fabricating a ring-shaped focused acoustic sensor with a concave detection surface. The other problem is the change of the optical penetration depth due to the optical scattering. To address this problem, it is necessary to calculate the optical penetration depth considering the optical scattering. In some cases, the effective attenuation coefficient calculated using Eq. (1) would be effective.

6. Conclusions

In this paper, we proposed a CWT-based method for quantifying the effective attenuation coefficients of optical absorbers using PA signals. Because this method uses the frequency instead of the amplitude to characterize the attenuation coefficient, it is unaffected by the fluence on the surface of the optical absorber. The CWT was used to calculate the time-resolved frequency spectra of PA signals, from which the maximum values of the dominant frequencies were calculated in turn. We demonstrated that the maximum values of the dominant frequencies of PA signals are linearly correlated with the effective attenuation coefficients of optical absorbers and, on the basis of this finding, the coefficients of the optical absorbers can be calculated to with mean square error of 2.0 cm^{-1}, which is much smaller than the errors obtained in calculating the quantified PPR.

We demonstrated that the CWT has advantages over the FT in terms of time resolution. The improved time resolution of CWT enables the separation of the PA signal from the residual oscillation in the time domain. The challenges of the proposed method are the effects of the excitation beam profile and optical absorber shape; to reduce such geometrical effects, we are fabricating a ring-shaped focused acoustic sensor with a concave detection surface.

This research was partially supported by a Health and Labor Science Research Grant for Research on Medical Device Development, JST Collaborative Research based on Industrial Demand (*In vivo* Molecular Imaging: toward Biophotonics Innovations in Medicine), and JSPS KAKENHI Grant No. 25750192. The authors appreciate the contributions of Mr. Y. Ikeda, Mr. H. Ishihara, Ms. M. Tanikawa, and Ms. Y. Mayumi to this study. Experiments were supported by the Laboratory Center, National Defense Medical College.

References

1. M. Xu and L. V. Wang, "Photoacoustic imaging in biomedicine," Rev. Sci. Instrum. **77**, 041101 (2006).
2. S. L. Jacques and S. A. Prahl, "Absorption spectra for biological tissues (Oregon Medical Laser Center, OR)" (2004), retrieved March 12, 2013, http://omlc.ogi.edu/spectra/.
3. J. Laufer, C. Elwell, D. Delpy, and P. Beard, "In vitro measurements of absolute blood oxygen saturation using pulsed near-infrared photoacoustic spectroscopy: accuracy and resolution," Phys. Med. Biol. **50**, 4409–4428 (2005).
4. A. Roggan, M. Friebel, K. Dorschel, A. Hahn, and G. Muller, "Optical properties of circulating human blood in the wavelength range 400–2500 nm," J. Biomed. Opt. **4**, 36–46 (1999).
5. M. Sivaramakrishnan, K. Maslov, H. F. Zhang, G. Stoica, and L. V. Wang, "Limitations of quantitative photoacoustic measurements of blood oxygenation in small vessels," Phys. Med. Biol. **52**, 1349–1361 (2007).
6. R. O. Esenaliev, I. V. Larina, K. V. Larin, D. J. Deyo, M. Motamedi, and D. S. Prough, "Optoacoustic technique for noninvasive monitoring of blood oxygenation: a feasibility study," Appl. Opt. **41**, 4722–4731 (2002).
7. B. Cox, J. G. Laufer, S. R. Arridge, and P. C. Beard, "Quantitative spectroscopic photoacoustic imaging: a review," J. Biomed. Opt. **17**, 061202 (2012).
8. Y. Wang and R. Wang, "Photoacoustic recovery of an absolute optical absorption coefficient with an exact solution of a wave equation," Phys. Med. Biol. **53**, 6167–6177 (2008).
9. Z. Guo, C. Favazza, A. Garcia-Uribe, and L. V. Wang, "Quantitative photoacoustic microscopy of optical absorption coefficients from acoustic spectra in the optical diffusive regime," J. Biomed. Opt. **17**, 066011 (2012).
10. J. Laufer, B. Cox, E. Zhang, and P. Beard, "Quantitative determination of chromophore concentrations from 2D photoacoustic images using a nonlinear model-based inversion scheme," Appl. Opt. **49**, 1219–1233 (2010).
11. J. A. Viator, S. L. Jacques, and S. A. Prahl, "Depth profiling of absorbing soft materials using photoacoustic methods," IEEE J. Sel. Top. Quantum Electron. **5**, 989–996 (1999).
12. M. Jaeger, M. Hejazi, and M. Frenz, "Diffraction-free acoustic detection for optoacoustic depth profiling of tissue using an optically transparent polyvinylidene fluoride pressure transducer operated in backward and forward mode," J. Biomed. Opt **10**, 024035 (2005).
13. Z. Guo, S. Hu, and L. V. Wang, "Calibration-free absolute quantification of optical absorption coefficients using acoustic spectra in 3D photoacoustic microscopy of biological tissue," Opt. Lett. **35**, 2067–2069 (2010).
14. T. Hirasawa, M. Ishihara, K. Tsujita, K. Hirota, K. Irisawa, M. Kitagaki, M. Fujita, and M. Kikuchi, "Continuous wavelet-transform analysis of photoacoustic signal waveform to determine optical absorption coefficient," Proc. SPIE **8223**, 822333 (2012).
15. T. Hirasawa, M. Fujita, S. Okawa, T. Kushibiki, and M. Ishihara, "Improvement in quantifying optical absorption coefficients based on continuous wavelet-transform by correcting distortions in temporal photoacoustic waveforms," Proc. SPIE **8581**, 85814J (2013).
16. S. H. Holan and J. A. Viator, "Automated wavelet denoising of photoacoustic signals for circulating melanoma cell detection and burn image reconstruction," Phys. Med. Biol. **53**, N227–N236 (2008).
17. J. A. Viator, B. Choi, M. Ambrose, J. Spanier, and J. S. Nelson, "In vivo port-wine stain depth determination with a photoacoustic probe," Appl. Opt. **42**, 3215–3224 (2003).
18. T. Lu, J. Jiang, Y. Su, Z. Song, J. Yao, and R. K. Wang, "Signal processing using wavelet transform in photoacoustic tomography," Proc. SPIE **6439**, 64390L (2007).
19. Z. Li, H. Li, Z. Zeng, W. Xie, and W. R. Chen, "Determination of optical absorption coefficient with focusing photoacoustic imaging," J. Biomed. Opt **17**, 061216 (2012).

20. Z. Li, H. Li, H. Chen, and W. Xie, "In vivo determination of acute myocardial ischemia based on photoacoustic imaging with a focused transducer," J. Biomed. Opt **16**, 076011 (2011).
21. S. A. Ermilov, R. Gharieb, A. Conjusteau, T. Miller, K. Mehta, and A. A. Oraevsky, "Data processing and quasi-3D optoacoustic imaging of tumors in the breast using a linear arc-shaped array of ultrasonic transducers," Proc. SPIE **6856**, 685603 (2008).
22. M. Ishihara, M. Sato, N. Kaneshiro, G. Mitani, S. Sato, J. Mochida, and M. Kikuchi, "Development of a diagnostic system for osteoarthritis using a photoacoustic measurement method," Lasers Surg. Med. **38**, 249–255 (2006).
23. C. Li and L. V. Wang, "Photoacoustic tomography and sensing in biomedicine," Phys. Med. Biol. **54**, R59–R97 (2009).
24. K. Irisawa, T. Hirasawa, K. Hirota, K. Tsujita, and M. Ishihara, "Influence of laser pulse width to the photoacoustic temporal waveform and the image resolution with a solid state excitation laser," Proc. SPIE **8223**, 82232W (2012).
25. V. Wilkens and C. Koch, "Amplitude and phase calibration of hydrophones up to 70 MHz using broadband pulse excitation and an optical reference hydrophone," J. Acoust. Soc. Am. **115**, 2892–2903 (2004).
26. A. Rosenthal, V. Ntziachristos, and D. Razansky, "Optoacoustic methods for frequency calibration of ultrasonic sensors," IEEE Trans. Ultrason. Ferroelectr. Freq. Control **58**, 316–326 (2011).
27. C. Torrence and G. P. Compo, "A practical guide to wavelet analysis," Bull. Am. Meteorol. Soc. **79**, 61–78 (1998).
28. P. Addison, J. Watson, and T. Feng, "Low-oscillation complex wavelets," J. Sound Vib. **254**, 733–762 (2002).
29. T. Kijewski and A. Kareem, "Wavelet transforms for system identification in civil engineering," Comput.-Aided Civil Infrastruct. Eng. **18**, 339–355 (2003).
30. P. S. Addison, *The Illustrated Wavelet Transform Handbook*, Introductory Theory and Applications in Science, Engineering, Medicine and Finance (IOP, 2005).

Comparison of regularization methods for photoacoustic image reconstruction

Shinpei Okawa, Takeshi Hirasawa, Toshihiro Kushibiki, and Miya Ishihara

Department of Medical Engineering, National Defense Medical College (Japan)

Keywords: Photoacoustic imaging, Inverse problem, Regularization

Introduction

Photoacoustic (PA) imaging obtains the distribution of the light absorbers. The energy of the light emitted by nano-second laser is absorbed by the light absorbers in tissues. And the energy is converted into heat, which causes elastic wave due to the thermal expansion. The detected elastict wave, PA signal namely, is used to reconstruct the PA image. The high resolution feature and the principle exploiting the absorption of the light allow us to obtain precise microvasular images[1].

By taking account of the excitation light propagation described by photon diffusion equation (PDE), the optical properties and concentrations of the light absorbers in optically inhomogeneous medium can be estimated by the PA image reconstruction. Laufer et al has proposed a model-based inversion scheme reconstructing the chromophore concentration[2]. The image reconstructed by solving the model-based inverse problem is always aggravated by noise and insufficient forward modeling due to the ill-posed nature. There exist mismatches between the actual measurement conditions and the forward model, which cause artifacts and low spatial resolution image.

In this paper, we compared regularization methods, i.e. truncated singular value decomposition (TSVD)[3], Tikhonov regularization and l_1 sparsity regularization[4], for model-based PA image reconstruction. The PA forward model was constructed by PA wave equation and PDE. The relation between the PA signals and the light absorption coefficient of the light absorber was formulated by finite element method (FEM). The effects of the regularization methods on the reconstructed images were investigated.

Image reconstruction method

The propagation of the PA wave is described by PA wave equation[1]. According to the PA wave equation, the intensity of the PA signal is linearly related to the source intensity. Therefore, we obtain a linear equation, $\mathbf{m} = L\mathbf{x}$, where $\mathbf{m}$ is the vector consists of the PA signals detected in multiple positions, and L is the system matrix relating $\mathbf{m}$ to the vector $\mathbf{x}$ of the source intensities at positions in the discretized medium. $\mathbf{x}$ is proportional to the product of the absorption coefficients μ_a and the fluence rates.

On the other hand, the propagation of the excitation light is described by PDE involving μ_a of the medium[4]. The fluence rate is calculated by solving PDE. When we assume that the medium has the background of the absorption coefficient μ_a^{bg} and the perturbation $\Delta\mu_a$ due to the existence of the strong light absorber such as tumor with angiogenesis, we obtain $\mu_a = \mu_a^{bg} + \Delta\mu_a$. By linearizing the relation of $\mathbf{x}$ to μ_a, the equation relating $\mathbf{m}$ to $\Delta\mu_a$ is formulated as,

$$\mathbf{m} - \mathbf{m}^{bg} = LJ\Delta\mu_a, \tag{1}$$

where $\mathbf{m}^{bg}$ is the contribution of μ_a^{bg} to $\mathbf{m}$, and J is the differential coefficients. By solving the equation for $\Delta\mu_a$ with given μ_a^{bg} and $\mathbf{m}^{bg}$, μ_a is reconstructed as the image. We prepared the matrices by use of FEM. Eq.(1) was solved with TSVD and with the nonlinear optimization scheme with minimizing 2-norm of $\mathbf{x}$ (Tikhonov regularization) and 1-norm of $\mathbf{x}$ (l_1 sparsity regularization).

Conditions of numerical experiment

The medium was a square region with 50 mm on a side. The light source with near-infrared wavelength was placed at (x, y) = (0 mm, 25 mm), and that 16 ultrasound detectors were placed from x = -14 to 16 mm on y = 25 mm with an equal spacing of 2 mm. The background medium had uniformly distributed with the scattering coefficient of 1.0 mm^{-1} and μ_a^{bg} = 0.001 mm^{-1}. The strong light absorber with μ_a = 0.01 mm^{-1} with 2 mm on a side was placed at (x, y) = (0 mm, 14 mm).
FEM was used with 10,201 nodes and 20,000 triangular elements to simulate PA signals. Gaussian noise was added to the simulated **m**. The noise had the standard deviation of 1 % of the maximum of the detected PA signals. The reconstruction was carried out on pixel basis. Single pixel had 2 mm on a side.

Results and discussions

Figure 1 shows the reconstructed images with TSVD, Tikhonov and l_1 sparsity regularizations. The strong absorber was reconstructed in the correct position by each regularization method. The area and the value of μ_a, however, were quite different. By TSVD and Tikhonov regularization, the area of the strong absorber was larger than true one, and the maximum value of the reconstructed μ_a was about 10 to 20 % of the true value. TSVD caused undulation in the reconstructed image. Tikhonov regularization provided the smooth distribution of μ_a.
On the other hand, l_1 sparsity regularization reconstructed image with high spatial resolution. The area of the strong absorber was correctly reconstructed. The value of the reconstructed μ_a was about 90 % of the true one. When prior information suggests that the true distribution of μ_a is sparse, l_1 sparsity regularization reconstructs more reliable PA image than TSVD and Tikhonov regularization does.

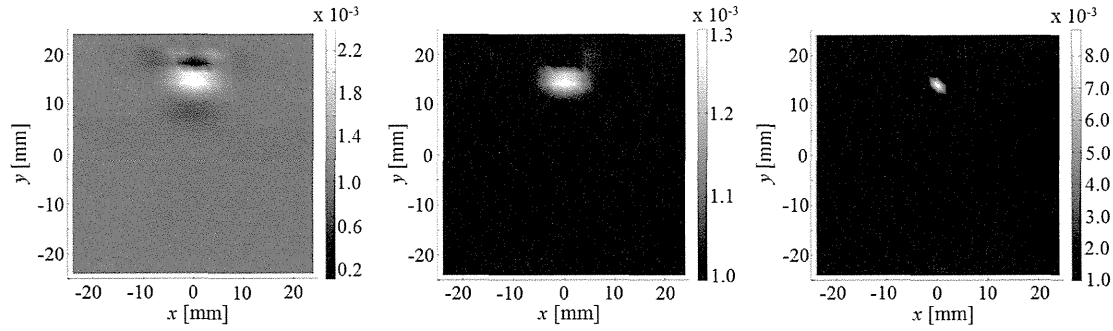

Fig. 1. Reconstructed PA images with TSVD method (left), Tikhonov regularization (center), and l_1 sparsity regularization (right).

Conclusion

The effects of the regularization methods for PA image reconstruction were compared. l_1 sparsity regularization reconstructs sparse distribution of the absorption coefficient, while TSVD and Tikhonov regularization obtain small changes in the absorption coefficient in broad area.

References

1) L. V. Wang *et al.*, Science, **335**, 1458-1462 (2012).
2) J. Laufer *et al.*, Appl. Opt., **49**, 1219-1233 (2010).
3) C. R. Vogel, Computational Methods for Inverse Problems, SIAM, (2002).
4) S. Okawa *et al.*, Biomed. Opt. Express, **2**, 3334-3348 (2012).